A multiscale micromechanical approach to model the deteriorating impact of alkali-silica reaction on concrete

Esposito, Rita; Hendriks, Max

DOI
10.1016/j.cemconcomp.2016.03.017

Publication date
2016

Document Version
Accepted author manuscript

Published in
Cement and Concrete Composites

Citation (APA)
Esposito, R., & Hendriks, M. (2016). A multiscale micromechanical approach to model the deteriorating impact of alkali-silica reaction on concrete. *Cement and Concrete Composites*, *70*(July), 139-152. https://doi.org/10.1016/j.cemconcomp.2016.03.017

A MULTISCALE MICROMECHANICAL APPROACH TO MODEL THE DETERIORATING IMPACT OF ALKALI-SILICA REACTION ON CONCRETE

Rita Esposito[a,*], Max A.N. Hendriks[a,b]

[a] *Delft University of Technology, Stevinweg 1, 2628 CN, Delft, The Netherlands.*
[b] *Norwegian University of Sciences and Technology (NTNU), Richard Birkelands vei 1a, 7491, Trondheim, Norway.*

Abstract

The alkali-silica reaction (ASR) in concrete is one of the most harmful deterioration processes, which leads to expansion and cracking of the material. To understand the evolution of ASR in concrete and its deteriorating impact on the material, a multiscale material model, from aggregate to concrete level, is proposed. The concrete, which at macro scale is considered a homogeneous material, is micromechanically modelled by a matrix-cracks system, in which each phase is uniform and behaves elastically. The damage criterion, associated to the cracks, is formulated on the basis of linear fracture mechanics theory. The model, which is analytically solved, is based on a limited numbers of input parameters, to be determined via micro and macro experimental investigations. The model is able to predict the non-linear behaviour of concrete subject to uniaxial loading in good agreement with code formu-

*Corresponding author. Tel.: +31 15 27 82537; fax: +31 15 27 85767.
Email address: r.esposito@tudelft.nl (Rita Esposito)

lations, which are usually input for numerical analyses of structures. For the case of ASR-affected material, the model overestimates the degradation rate of mechanical properties as a function of the expansion. On the contrary, the relationship between stiffness and strength deterioration is correctly approximated. Various model modifications are explored suggesting that the assumption of elastic behaviour of each phase should be reconsidered.
Keywords: Alkali-silica reaction (ASR), Concrete, Chemo-Mechanical Processes, Mechanical Properties, Multiscale Material Modelling, Microporomechanics, Two-Scale Double Porosity System

---

1. BACKGROUND AND SIGNIFICANCE

The alkali-silica reaction (ASR) in concrete evolves at different material levels. The chemical process (Glasser, 1992) involves silica ions, available in the aggregates, and alkali ions mainly present in pores solution (reaction products level). The formed alkali-silica gel, when exposed to moisture, tends to swell. Its expansion, while confined in the pore structure of concrete, builds up an internal pressure with the consequent formation of cracks in the aggregates and in the cement paste (aggregate level). As a result, the concrete is expanding and its mechanical properties are degrading (concrete level), (see Esposito et al. (2015) where the work of 12 researchers is statistically evaluated). The reduction in material resistance compromises the performance of the structure in terms of both capacity and durability (structural level).

The interaction of the various phenomena at the different levels is a particular characteristic of ASR. The applied external load substantiated by an

affected structures can be redistributed due to the differential resistance of the material (structural-to-concrete level interaction). The stress state of the material influences the redistribution of the gel (Multon and Toutlemonde, 2006; Saouma and Perotti, 2006), thus the expansion and the cracking formation (concrete-to-aggregate level interaction). Eventually, the redistribution of cracks modifies the equilibrium of the system at the reaction products level, thus the chemical process can be (re)activated or stopped (aggregate-to-reaction products level interaction).

Due to the multiscale nature of the phenomenon, the problem has been studied by different experts (e.g. geologists, material engineers, structural engineers) in different fields (e.g. material sciences, structural mechanics) resulting in several modelling approaches with different aims. Earlier approaches focussed on the description of the structural behaviour by imposing an ASR expansion at concrete level (Charlwood, 1994; Léger et al., 1996). Due to their easy application, they became popular in the engineering practice and were implemented in various finite element softwares. Their development followed a phenomenological approach; thermodynamic concepts were introduced to describe the thermo-chemo-mechanical coupling (Ulm et al., 2000; Capra and Sellier, 2003; Bangert et al., 2004; Saouma and Perotti, 2006). Thanks to the technological advancement in microscopic investigation, the attention moved to the aggregate level. The effect of alkali-silica gel swelling on concrete was considered as an internal pressure. The various pressure-based models can be divided in two categories: analytical approaches following the fracture mechanics theory (Bažant et al., 2000; Reinhardt and Mielich, 2011; Dormieux et al., 2004) and computational ap-

proaches adopting finite element analyses at aggregate level (Comby-Peyrot et al., 2009; Schlangen and Copuroğlu, 2010; Anaç et al., 2012; Wu et al., 2014). To couple the physical chemistry of ASR with the mechanical behaviour of concrete, various modelling approaches have studied the phenomenon at reaction products level, by considering the mass production of the alkali-silica gel as a driving parameter. These were mainly a refinement of the previous developed pressure-based model. Again both analytical (Ulm et al., 2002; Lemarchand et al., 2005; Charpin and Ehrlacher, 2012) and computational (Grimal et al., 2008; Dunant and Scrivener, 2010; Giorla et al., 2015; Pignatelli et al., 2013) approaches were adopted. The study of the chemical process which leads to the swelling of the gel and the expansion of concrete was the focus of the last two decades. Model based on the diffusion and reaction of the ions were first developed in a mathematical framework (Bažant and Steffens, 2000; Suwito et al., 2002; Liuaudat et al., 2014) and subsequently implemented in finite element software to describe the mechanical impact (Poyet et al., 2007; Multon et al., 2009; Sanchez et al., 2014; Alnaggar et al., 2013).

To understand the evolution of ASR in concrete and its degradation impact on the material, in this paper a multiscale material model is proposed. The model ranges from the aggregate level (also known as meso level) to the concrete level. It is a pressure-based model, based on the microporomechanics theory developed by Dormieux et al. (2006). A similar approach was previously adopted by Lemarchand et al. (2005) and by Charpin and Ehrlacher (2014) to describe, respectively, the expansion behaviour of ASR-affected concrete in free-expansion and under confined conditions, without concern-

ing for the mechanical degradation of concrete. The model presented in this paper aims to describe the deteriorating impact of ASR on concrete in terms of the relation between the induced expansion and the degradation of mechanical properties.

The proposed model is developed in an analytical framework and is based on a limited number of input parameters, which can be determined via microscopic and macroscopic laboratory investigation (e.g. porosity measurements and mechanical tests). As a result of these characteristics, it is envisioned that the proposed model can be extended to range from the reaction products level to the structural levels. To extend it to the reaction product level, a kinetic formulation should be introduced, which can be either expressed in terms of gel mass production or on the basis of the ions diffusion-reaction process. To extend it to structural level, the model can be implemented in a finite element software at integration point level or it can be adopted as tool for the definition of the constitutive laws for structural analyses.

The model, which is first validated for the case of concrete subjected to only external loading, is applied to describe the deteriorating impact of ASR on concrete in unconstrained specimens. The attention is focussed on the relation between concrete expansion and the degradation of engineering properties (e.g. elastic modulus, tensile strength, compressive strength). Laboratory tests performed on a recovered concrete mix from the highly affected Nautesund bridge (Norway) are adopted for comparison.

2. MULTISCALE MATERIAL MODEL

The presented multiscale material model describes the macroscopic degradation behaviour of concrete on the basis of micromechanical aspects. The concrete is modelled as an heterogeneous material at microscopic level and its macroscopic properties are evaluated considering a representative elementary volume (REV).

2.1. Micromechanical Model

At aggregate level (commonly referred to as the meso level of cementitious materials), the concrete is modelled as a matrix-inclusions system, in which each phase is homogeneous and behaves elastically. The concrete is composed by cracks embedded in a solid matrix, as shown in Figure 1a. The solid matrix is constituted by aggregates embedded in the cement paste (Figure 1b). Consequently, no explicit distinction is made between cracks in the aggregates or in the cement paste. The aggregates are modelled as spherical inclusions having a volume fraction ϕ_{agg}.

Three orthogonal families of cracks are considered ($m = 3$). Within each family the cracks are aligned in one plane with normal $\boldsymbol{n}_i$. Algorithmically, there is no limit to the number of planes (e.g. Bažant and Oh (1983b) adopt 21 families of aligned cracks in their microplane models). The cracks of the i-th family are represented by penny-shaped inclusions, with radius a_i in the inclusion's plane and radius c_i in thickness direction (or crack opening $2c_i$). Their aspect ratio X_i and volume fraction $\phi_{\text{c}i}$ are defined as:

$$X_i = \frac{c_i}{a_i} \tag{1a}$$

$$\phi_{ci} = \frac{4}{3}\pi c_i n_i a_i^2 \tag{1b}$$

where n_i is the number of cracks per unit of volume. The aspect ratio X_i and the volume fractions ϕ_{ci} are the main parameters describing the microstructural evolution. As a result, the intrinsic values of the crack radius a_i, the crack opening $2c_i$ and the number of cracks n_i have a limited physical meaning. All crack families contribute to the porosity of concrete, which has a volume fraction Φ equal to:

$$\Phi = \sum_{i=1}^{m} \phi_{ci} \tag{2}$$

The volume fraction of the solid matrix ϕ_{m} results:

$$\phi_{\mathrm{m}} = 1 - \Phi \tag{3}$$

Considering the crack propagation for the i-th family within the elastic solid matrix, the damage state is identified adopting the crack density variable ϵ_i (Budiansky and O'Connell, 1976):

$$\epsilon_i = n_i a_i^3 = \frac{3\phi_{\mathrm{ci}}}{4\pi X_i} \tag{4}$$

The last expression in Eq. 4 shows that the damage evolution does not depend on the specific value of the crack radius a_i, but that it is influenced by the aspect ratio X_i and the volume fraction ϕ_{ci} of the cracks. This observation is only valid for the current proposed model. For approaches modelling nucleation of cracks or opening/closing of cracks and for models accounting

for transport phenomena specific value of crack radius a_i, crack opening $2c_i$ and number of cracks n do matter.

2.2. State Equations and Damage Criterion

The concrete can be subjected both to an external load (e.g. a uniform macroscopic strain $\boldsymbol{E}$) and to the internal pressure P, which is developed by the confined swelling of expansive alkali-silica gel in the cracks. In this first approach the problem is solved within the framework of fully saturated porous media, considering the long term nature of the process. The state equations which characterize the linear poroelastic behaviour of the REV are described in agreement with Dormieux et al. (2006):

$$\boldsymbol{\Sigma} = \mathbb{C} : \boldsymbol{E} - \boldsymbol{B}P \tag{5a}$$

$$\Phi - \Phi^* = \boldsymbol{B} : \boldsymbol{E} + \frac{P}{N} \tag{5b}$$

where $\mathbb{C}$ is the effective drained stiffness tensor, $\boldsymbol{B}$ and $1/N$ are the Biot tensor and moduli respectively, $\boldsymbol{\Sigma}$ is the macroscopic stress and $\Phi - \Phi^*$ is the elastic deformation of the total porosity, which initial value is equal to Φ^*.

The effective drained stiffness tensor $\mathbb{C}$ is evaluated through the Mori-Tanaka homogenization scheme (Benveniste, 1987), considering a two-phase system composed by the solid matrix and the cracks (Figure 1a):

$$\mathbb{C} = \mathbb{C}_{\mathrm{m}} + \sum_{i=1}^{m} \phi_{\mathrm{c}i} \left(\mathbb{C}_{\mathrm{c}i} - \mathbb{C}_{\mathrm{m}} \right) : \mathbb{A}_{\mathrm{c}i} \tag{6}$$

where $\mathbb{C}_{\mathrm{m}}$ and $\mathbb{C}_{\mathrm{c}i}$ are the stiffness tensors of the solid matrix and of the i-th crack family, respectively. The strain concentration tensor for the i-th crack family $\mathbb{A}_{\mathrm{c}i}$ is defined as:

$$\mathbb{A}_{\mathrm{c}i} = \mathbb{T}_{\mathrm{c}i} : \left(\phi_{\mathrm{m}} + \sum_{j=1}^{m} \phi_{\mathrm{c}j} \mathbb{T}_{\mathrm{c}j} \right)^{-1} \tag{7}$$

with $\mathbb{T}_{\mathrm{c}i}$ equal to its dilute estimate:

$$\mathbb{T}_{\mathrm{c}i} = \left[\mathbb{I} + \mathbb{S}_{\mathrm{c}i} : \mathbb{C}_{\mathrm{m}}^{-1} : (\mathbb{C}_{\mathrm{c}i} - \mathbb{C}_{\mathrm{m}}) \right]^{-1} \tag{8}$$

being $\mathbb{S}_{\mathrm{c}i}$ the Eshelby tensor, which depends on the shape of the cracks X_i and on the Poisson ratio of the solid matrix ν_{m} (Mura, 1987). The cracks are considered as empty inclusions with no stiffness; thus Eqs. 6-8 can be reduced by substituting $\mathbb{C}_{\mathrm{c}i}$ with the null tensor $\mathbb{O}$.

The stiffness tensor of the solid matrix $\mathbb{C}_{\mathrm{m}}$ is likewise evaluated with Eqs. 6-8, considering a two-phase system composed by the cement paste and the aggregates (Figure 1b). Its value is kept constant during the crack propagation. As a consequence, no distinction is made between damage propagation in the aggregate and in the cement paste and the micromechanical formulation results in a one-scale single porosity model.

The Biot tensor $\boldsymbol{B}$ and modulus N for a porous medium read (Dormieux et al., 2006):

$$\boldsymbol{B} = \boldsymbol{I} - \mathbb{C}_{\mathrm{m}}^{-1} : \mathbb{C} : \boldsymbol{I} = \boldsymbol{I} - \mathbb{C} : \mathbb{C}_{\mathrm{m}}^{-1} : \boldsymbol{I} \tag{9a}$$

$$\frac{1}{N} = (\boldsymbol{B} - \Phi^{*} \boldsymbol{I}) : \mathbb{C}_{\mathrm{m}}^{-1} : \boldsymbol{I} \tag{9b}$$

The approach results in a three-dimensional smeared model where the macroscopic stress and strain are obtained as an average of the microscopic quantities. It is noted that the resulting stiffness tensor is a function of the elastic properties of each phase and of the volume fraction, the shape, the orientation and the alignment of the inclusions. It is not influenced from the position and the size of the inclusions.

The damage criterion is formulated in the framework of linear fracture mechanics theory, on the basis of thermodynamic concepts (Dormieux et al., 2006). The damage process is simulated by means of cracking propagation. Nucleation and opening/closing of the cracks are not accounted. As a consequence, the crack density variable ϵ_i of the i-th crack family (Eq. 4) is increasing by an increment of the crack radius a_i, while the number of cracks per unit of volume n_i and the crack opening $2c_i$ are constant.

Considering the energy release G_i as the driving force of the damage process, the damage criterion reads:

$$G_i - G_{ci} \leq 0; \quad \dot{\epsilon}_i \geq 0; \quad (G_i - G_{ci})\,\dot{\epsilon}_i = 0 \tag{10}$$

where G_{ci} is its critical value. The energy release rate G_i represents the macroscopic dissipation, which is a function of the potential energy of the system Ψ_{pot}:

$$G_i\left(\boldsymbol{E}, P, \epsilon_i\right) = \frac{\partial \Psi_{\text{pot}}}{\partial \epsilon_i} = -\frac{1}{2}\left\langle \boldsymbol{E} + P\mathbb{C}_0^{-1} : \boldsymbol{I} \right\rangle : \frac{\partial \mathbb{C}\left(\epsilon_i\right)}{\partial \epsilon_i} : \left\langle \boldsymbol{E} + P\mathbb{C}_0^{-1} : \boldsymbol{I} \right\rangle \tag{11}$$

where $\boldsymbol{E} + P\mathbb{C}_0^{-1} : \boldsymbol{I} = \boldsymbol{E}'$ is the effective strain controlling the damage. In

order to capture the different damage mechanisms developed under tension and compression loading (Esposito, 2015), the positive part of the effective strain $\langle \boldsymbol{E} \rangle$ has be considered following Mazars (1986).

The critical energy release rate G_{ci} can be expressed as function of the current damage parameter ϵ_i:

$$G_{ci} = \frac{2\pi}{3} g_{\mathrm{f}} \left(\frac{n_i}{\epsilon_i} \right)^{1/3} = \frac{2\pi}{3} \frac{g_{\mathrm{f}}}{a_i} \tag{12}$$

with g_{f} the microscopic fracture energy, which is a constant material parameter.

3. THE CASE STUDY

In order to validate the model, a selected case study, which represents the concrete mix used in the severely affected Nautesund bridge (Norway), is presented. Through a collaboration between the Delft University of Technology (TU Delft) and the Norwegian Roads Public Administration (NPRA), microscopic and macroscopic investigation were performed both on extracted pieces of the bridge and on recovered laboratory samples. The Norwegian aggregates were mainly composed of coarse grained quartz, quartzite, gneiss, metarhyolite and other minor rock types. The maximum diameter was 22 mm. It was estimated that 33% of aggregates with size 0-8 mm and 36% of coarse gravel were potentially alkali reactive. The adopted mix proportion cement/fine aggregates/coarse aggregates/water, by weight, were 1:3.03:1.74:0.45. NORCEM Industri cement CEM I 42.5R with a dosage of 380 kg/m^3 and an equivalent Na_2O_{eq} content of 1.17% was used. Dry aggregates were used in the concrete mix.

The expansion was determined on three prisms of size 75x75x280 mm by following the measurement procedure proposed by RILEM recommendation AAR-3 (RILEM TC 219-ACS, 2011). Destructive tests were performed at predefined time intervals on companion specimens stored in similar conditions (T = 38 °C and RH = 96%). The static elastic modulus Y and the prismatic compressive strength f_{c} were determined on prisms 100x100x400 mm in agreement with ISO 1920-10:2010(E) (ISO, 2010). The splitting tensile strength $f_{\mathrm{t,sp}}$ was measured on cubes with side of 150 mm in agreement with EN 13290-6:2009 (NEN, 2009). The 28-day cubic compressive strength f_{cc} was measured on 150 mm cube specimens stored at 20 °C in a foggy room (NEN, 2002) and it was equal to 64.11 MPa.

Figure 2 reports the degradation of mechanical properties in terms of normalised values versus expansion. Each normalised value is obtained as the ratio between the current value and its reference one (Esposito et al., 2015). The reference value is defined as the interpolated value corresponding to an expansion equal to 0.05% (Y^{ref} = 26130 MPa, $f_{\mathrm{c}}^{\mathrm{ref}}$ = 61.23 MPa, and $f_{\mathrm{t,sp}}^{\mathrm{ref}}$ = 3.85 MPa).

The elastic modulus shows the highest degradation reaching a minimum value of 67%. The splitting tensile strength degrades to a minimum value of 84%. On the contrary, the compressive strength does not show any degradation. The results are in line with findings from other experimental data available in literature and normalised with the same procedure (Esposito et al., 2015; Esposito, 2015).

4. DEGRADATION DUE TO EXTERNAL LOAD

The model is validated first for the case of concrete subjected to external mechanical loading, simulating uniaxial tensile and compressive tests. The results are compared with analytical formulations proposed by the Model Codes (*fib*, 2011; CEB-FIP, 1993). The analyses simulate the concrete of the case study presented in Section 3. The identification of the model parameters is presented first, followed by the simulation of the uniaxial tests and a concise sensitive study.

4.1. Input and Calibrated Parameters

Table 1 lists the input and calibrated parameters of the model. They define the initial microstructure of the concrete, the elastic constants of each phase and the microscopic fracture energy g_{f}.

In general the input parameters of the model can be determined by macroscopic and microscopic investigation, considering well-known properties correlation (e.g. Power's law for the determination of the capillary porosity from w/c ratio and hydration degree or Eurocode 2 formulas for correlation between 28-day mechanical properties). In the present case the elastic modulus Y_{in} and tensile strength $f_{\mathrm{t,in}}$ of the undamaged concrete are calculated from 28-day cubic compressive strength (Eurocode 2, 2005), as reported in Section 3. The aggregate elastic modulus Y_{agg} has been determined by nanoindentation test. The elastic modulus of the cement paste Y_{cem} has been arbitrary chosen twice smaller than the one of the aggregates; this value accounts also for the intrinsic porosity of concrete that does not contribute to the cracking. For both phases, the Poisson ratio $\nu_{\mathrm{cem}} = \nu_{\mathrm{agg}}$ is equal to 0.20.

The volume fraction of the aggregates ϕ_{agg} is determined by mixture proportion. For undamaged concrete, it is assumed that the three cracks families are identical in aspect ratio $X_{\text{in}} = X_{1,\text{in}} = X_{2,\text{in}} = X_{3,\text{in}}$ and volume fraction $\phi_{\text{c,in}} = \phi_{\text{c1,in}} = \phi_{\text{c2,in}} = \phi_{\text{c3,in}}$. Consequently, the undamaged concrete results as a nearly isotropic material (Esposito, 2015). The crack opening $2c$ is assumed constant and equal to 0.10 mm. The total initial volume fraction of the cracks is arbitrary set to 70% of the capillary porosity calculated with Power's law ($\Phi_{\text{in}} = 0.70\,\Phi_{\text{in}}^{\text{Power}}$), because not all the capillary pores will become cracks and contribute to the damage. The influence of the input parameters is shown in the parametric study presented in Section 4.3.

The calibration process is subdivided in two parts: first the calculation of the initial aspect ratio of the cracks X_{in} second the determination of the microscopic fracture energy g_{f}. The stiffness tensor of the solid matrix $\mathbb{C}_{\text{m}}$ is calculated with equations similar to Eqs. 6-8. By imposing that the elastic modulus of the concrete is equal to the one of the undamaged concrete Y_{in}, the initial aspect ratio X_{in} is calibrated. Consequently, the crack radius $a_{\text{in}} = a_{1,\text{in}} = a_{2,\text{in}} = a_{3,\text{in}}$ and number of cracks per unit of volume $n = n_1 = n_2 = n_3$ can be calculated by Eq. 1. The initial damage state $\epsilon = \epsilon_1 = \epsilon_2 = \epsilon_3$ can be calculated by Eq. 4. The microscopic fracture energy g_{f} is derived by imposing that the cracks of the i-th family, with initial radius $a_{i,\text{in}}$ will start to propagate in a uniaxial tensile test, for a uniaxial macroscopic stress equal to the tensile strength of undamaged concrete:

$$G_i\left(\boldsymbol{E} = \mathbb{C}^{-1} : \boldsymbol{\Sigma}^{\text{cr}}, P = 0, \epsilon_i = \epsilon_{i,\text{in}}\right) := G_{\text{c}i}\left(\epsilon_i = \epsilon_{i,\text{in}}, g_{\text{f}}\right) \tag{13}$$

where the only no zero component of the stress tensor $\boldsymbol{\Sigma}^{\text{cr}}$ is $\Sigma_{ii}^{\text{cr}} = f_{\text{t,in}}$.

4.2. Uniaxial Loading Tests

The multiscale material model is applied to simulate the degradation of concrete under uniaxial load. The macroscopic stress $\boldsymbol{\Sigma}$ is determined by Eq. 5 with $P = 0$ and $\boldsymbol{E} = \boldsymbol{E}^{\text{applied}}$.

Figure 3 shows the resulting non-linear behaviour of concrete subjected to external uniaxial tensile and compressive load. The model results are compared with the analytical formulations proposed by the Model Codes (*fib*, 2011; CEB-FIP, 1993), which are based on a statistically large number of experimental tests.

In the case of tension loading along the 3-axis (Figure 3a), a softening curve is obtained which resembles the so-called exponential softening curve, frequentlly used in numerical models of concrete at structural level. The damage propagation starts after the maximum load is achieved (Figure 3c); only the cracks perpendicular to the load direction are propagating ($a_3 > a_{\text{in}}$, $a_1 = a_2 = a_{\text{in}}$). The peak stress is retrieved equal to the tensile strength of undamaged concrete $f_{\text{t,in}}$, as imposed by the calibration of the microscopic fracture energy g_{f} (Section 4.1). The macroscopic fracture energy G_{f} can be estimated, from the simulation, calculating the area underneath the stress-strain curve A_{t}. Considering that the model represents the behaviour of concrete in the fracture zone, the area A_{t} is multiplied by three times the maximum aggregate size d_{max} (Bažant and Oh, 1983a), as reported in Table 2. The resulting macroscopic fracture energy is close to the estimation provided by the Model Codes (*fib*, 2011; CEB-FIP, 1993).

In the case of compressive loading along the 3-axis (Figure 3b), a stiffening-softening relation is obtained which resembles well-known parabolic softening

curves, prescribed by codes and frequently used in numerical models of concrete at structural level. The cracks are now developing in the two planes aligned with the load direction ($a_3 = a_{\text{in}}$, $a_1 = a_2 > a_{\text{in}}$); due to the identical initial shape of the cracks, the propagation is similar for the two families (Figures 3d). This crack pattern resembles the splitting cracks usually observed in concrete specimens tested under uniaxial compression. The damage propagation starts at a stress $\Sigma_{33}^{\text{prop}} = -19.66$ MPa (Table 2). The obtained peak stress $\Sigma_{33}^{\text{peak}} = -53.29$ MPa is close to the compressive strength of concrete. The ratio $\Sigma_{33}^{\text{prop}}/\Sigma_{33}^{\text{peak}} = 0.36$ is close to the ratio 1/3 proposed by the Model Codes (*fib*, 2011; CEB-FIP, 1993). The obtained results in terms of stress-strain curve, are in good agreement with the relationships proposed by the Model Codes (*fib*, 2011; CEB-FIP, 1993).

In conclusion, the model is able to approximate the known stress-strain relationship of concrete under tensile and compressive loading, with a limited number of input parameters. It is noted that only the elastic branch in tension is a direct result of calibration. The non-linear softening curve in tension and the entire curve in compression are a direct result of the model. The analytical relations have been derived from a large number of experimental campaigns and worldwide recognized by the scientific community. This proves the validity of the model's hypotheses as well as the calibration procedure.

4.3. Parametric Study

The model input parameters, Table 1, can be divided in three categories: one for the macroscopic properties of undamaged concrete (Y_{in}, $f_{\text{t,in}}$), one related to the solid matrix (Y_{cem}, Y_{agg}, $\nu_{\text{cem}} = \nu_{\text{agg}}$, ϕ_{agg}) and one to define

the initial status of cracks (Φ_{in}, c). They can be determined via macro to microscopic investigation, such as mechanical tests, nano-indentation tests and porosity measurements.

The macroscopic properties of undamaged concrete (Y_{in}, $f_{\text{t,in}}$) and the volume fraction of aggregates (ϕ_{agg}) are considered as known and fixed for the analysed case. A parametric study is performed on the remaining variables varying them one by one (Figure 4). Each time the calibration procedure is repeated.

The solid matrix is defined by the aggregates embedded in the cement paste. Its properties remain constant during the damage evolution. Thus, rather than the properties of aggregate and cement paste, the elastic constants of the solid matrix are relevant. Its mechanical properties are related to: the volume fraction of the aggregates ϕ_{agg}, the elastic modulus of the cement paste Y_{cem}, the elastic modulus of the aggregates Y_{agg} and the Poisson ratio of both phases $\nu_{\text{cem}} = \nu_{\text{agg}}$. Knowing the amount of aggregates by mix design, the ratio between the elastic moduli of each phase $Y_{\text{cem}}/Y_{\text{agg}}$ and their Poisson ratio $\nu_{\text{cem}} = \nu_{\text{agg}}$ define the stiffness tensor of the solid matrix $\mathbb{C}_{\text{m}}$.

Figures 4a and 4b present the sensitivity of the model with respect to the ratio between the elastic moduli of cement paste and aggregates $Y_{\text{cem}}/Y_{\text{agg}}$, by varying Y_{cem}. The higher is this ratio, the stiffer is the solid matrix. As a consequence, the calibration against the macroscopic stiffness Y_{in} leads to more elongated penny-shaped initial cracks ($a_{\text{in}} \gg c$). The calibration against the macroscopic strength $f_{\text{t,in}}$ subsequently leads to a higher microscopic fracture energy g_{f} (Figure 4a). The resulting non-linear behaviour of concrete

is strongly affected by the elastic modulus of the solid matrix (Figure 4b). In the case of tension loading, the ultimate strain, and consequentially the macroscopic fracture energy G_{f} results higher for a stiffer solid matrix. In the case of compression loading, a substantial variation is observed. For a stiffer solid matrix, the cracks propagate later and the peak stress $\Sigma_{33}^{\mathrm{peak}}$ is higher; furthermore the ratio $\Sigma_{33}^{\mathrm{prop}}/\Sigma_{33}^{\mathrm{peak}}$ decreases.

Figures 4c and 4d present the influence of Poisson ratios of aggregate and cement paste. Their values are assumed equal. As a consequence of the adopted homogenization method (Eqs. 6-8) and of the modelling choices (the aggregates are considered as spherical inclusions), the solid matrix has the same Poisson ratio as its phases ($\nu_{\mathrm{m}} = \nu_{\mathrm{cem}} = \nu_{\mathrm{agg}}$). This elastic constant has a limited influence on both the calibrated parameters and the behaviour of the overall material under uniaxial loading. Its influence can be mainly appreciated for the behaviour of concrete under compressive load, because the Poisson ratio correlates the lateral and applied normal strains.

In Figures 4e and 4f the influence of the last category of input parameters is presented, focusing the attention on the initial volume fraction of cracks Φ_{in}. Considering the model assumptions, the following correlation holds between the initial aspect ratio X_{in} and the initial volume fraction Φ_{in} for the same overall stiffness tensor $\mathbb{C}_{\mathrm{in}}$: the higher is the initial volume fraction ($\Phi_{\mathrm{in}} \uparrow$), the higher is the initial aspect ratio ($X_{\mathrm{in}} \uparrow$); thus, the inclusions tend to have a more spheroidal shape ($a_{\mathrm{in}} \to c_{\mathrm{in}}$). If the crack opening $2c$ is assumed constant ($c = c_{\mathrm{in}}$), the relationship can be expressed in terms of the initial crack radius a_{in} in the major directions, as shown in Figure 4e. A similar trend is observed for the microscopic fracture energy g_{f}. The

initial volume fraction of the cracks Φ_{in} influences the non-linear behaviour of concrete similarly to the ratio between the elastic moduli of cement paste and aggregate $Y_{\text{cem}}/Y_{\text{agg}}$ (compare Figures 4b and 4f). In fact, an initial lower amount of cracks, which tend to be elongated penny-shaped inclusions ($a_{\text{in}} \gg c$), leads to an overestimation of the compressive strength and of the macroscopic fracture energy.

Note that crack opening $2c$ affects the initial crack density variable (Eqs. 1 and 4), but it is not relevant in the damage evolution. In fact, being constant the number of crack per unit of volume n, the ratio between the crack density variable ϵ and its initial value ϵ_{in} results only a function of the crack radius a (Esposito, 2015). It is noted that fluid and alkali transport in concrete are outside the scope of this paper. For these phenomena the value of the crack opening $2c$ is important.

Concluding, the elastic modulus of the solid matrix, Y_{m}, expressed as a function of the ratio $Y_{\text{cem}}/Y_{\text{agg}}$ and the initial porosity Φ_{in}, can influence the non-linear model behaviour of concrete under uniaxial external loading. The Poisson ratio of the solid matrix ν_{m} has a limited influence, which can be noticed only for the behaviour under compressive loading. On the contrary, the damage process does not depend on the crack opening $2c$.

5. DEGRADATION DUE TO INTERNAL PRESSURE

The ASR process is simulated considering that the expansive alkali-silica gel saturates the concrete porosity and induces a pressure P. In the case of free-expansion of concrete, this phenomenon is macroscopically stress-free ($\boldsymbol{\Sigma}$) and the macroscopic strain $\boldsymbol{E} = \boldsymbol{E}^{\text{p}}$ is derived from Eq. 5:

$$\boldsymbol{\Sigma} = 0 \quad \Rightarrow \quad \boldsymbol{E} = \boldsymbol{E}^{\mathrm{p}} = \mathbb{C}^{-1} : \boldsymbol{B} P \tag{14}$$

The model is applied to simulate the degradation behaviour observed for the case study presented in Section 3. The input and calibrated parameters were listed in Table 1.

Figure 5 shows the relationship between the crack radius a, the macroscopic strain $\boldsymbol{E} = \boldsymbol{E}^{\mathrm{p}}$ and the pressure P. The radii a_i develop equally, due to the equal initial values and symmetry of the loading conditions. For the same reasons, the strains E_{11}, E_{22} and E_{33} develop equally. In the initial state the cracks are empty and the alkali-silica gel does not pressurize the concrete porosity ($P = 0$), resulting in zero macroscopic deformation ($\boldsymbol{E} = 0$). The saturation of the porous medium is assumed instantaneous, resulting in an increase of pressure P and macroscopic strain $\boldsymbol{E}$ for the initial crack radius. While the damage process evolves, thus for increasing values of crack radius a, the stiffness $\mathbb{C}$ decreases (Eq. 6) and the Biot tensor $\boldsymbol{B}$ increases (Eq. 9). As a consequence the pressure P, needed for further damaging the system, decreases and the macroscopic expansion strain $\boldsymbol{E}^{\mathrm{p}}$ increases.

To study the effect of ASR on the material deterioration, subsequent uniaxial tests have been simulated at eight levels of expansion $\boldsymbol{E}^{\mathrm{p}}$ (Figure 6). In this case, the macroscopic strain $\boldsymbol{E}$ is the sum of the expansion strain $\boldsymbol{E}^{\mathrm{p}}$ and of the applied one $\boldsymbol{E}^{\mathrm{applied}}$. The case of unaffected concrete ($E^{\mathrm{p}}_{33} = 0$), is the same as presented in Figure 3.

For affected concrete, the expansion strain E^{p}_{33} causes that the stress-strain curves appears as shifted on the horizontal axis. The curves present a similar shape, composed by linear and softening/hardening branches. Ana-

lysing Eq. 10 together with Eq. 11, it is concluded that the linear stage represents a transition phase, characterized by no further crack propagation, in which the applied load reduces the internal pressure down to zero.

Due to the damage induced by the pressure P the stiffness in the linear stage is lower with respect to the one of unaffected concrete. Consequently, the peak stress is reduced both in tension and compression.

Figure 7 shows that the crack opening $2c$ slightly varies as a function of the macroscopic strain $\boldsymbol{E}$ during the uniaxial compressive tests. Its value has been post-processed as a function of the local strain in the inclusions as proposed by Deude et al. (2001):

$$c_i = c_{i,\text{in}} \left(1 + \boldsymbol{n}_i \cdot \boldsymbol{\varepsilon}_i \cdot \boldsymbol{n}_i\right) = c_{i,\text{in}} \left(1 + \boldsymbol{n}_i \cdot \mathbb{A}_i : \boldsymbol{E} \cdot \boldsymbol{n}_i\right) \leq c_{i,\text{in}} \tag{15}$$

where $c_{i,\text{in}}$ is the initial value of 0.1 mm. The results indicate that the cracks are far from a complete closure, thus including the opening/closing phenomenon of the cracks in the model will not show any appreciable difference.

Figure 8 compares the model and experimental results in terms of mechanical properties degradation. The property values are normalised with respect to their initial value for the model results; the normalisation procedure for the experimental results has been presented in Section 3. The model overestimates the degradation of all the properties, in correlation with the expansion (Figure 8a). The model is able to simulate the degradation rate between stiffness and strengths, as shown in Figure 8b.

The multiscale material model, which appears successfully in the evaluation of concrete behaviour under uniaxial external loading and correctly approximates the relationship between stiffness and strength degradation in

ASR affected concrete, requires improvement to correctly estimate the relationship between expansion and stiffness degradation. In the next section, possible modifications of the proposed model are explored.

6. MODEL MODIFICATIONS

In Section 2 a multiscale material model based on a single porosity system has been presented. It assumes a porosity system composed by three penny-shaped crack families embedded into a solid matrix, which constituents are aggregates and cement paste.

The model is able to predict the behaviour of concrete under uniaxial tensile and compressive loads, capturing not only the peaks stress, but also its main non-linear characteristics such as the softening/hardening shape, ultimate strain and macroscopic fracture energy G_{f}.

When applied to the case of ASR-affected concrete, the model is able to determine the correlation between pressure P and expansion strains $\boldsymbol{E}^{\mathrm{p}}$. The degradation of mechanical properties in ASR-affected concrete under free-expansion conditions, are determined by simulating subsequent uniaxial tests. The relation between stiffness and strengths is predicted reasonable well. However, the model overestimates the degradation in stiffness as a function of expansion. In this section, three model modifications are explored.

6.1. Microscopic Fracture Energy as Input Parameter

The microscopic fracture energy g_{f} together with the crack density variable ϵ governs the fracture process. The latter is a state variable, while the former is a constant. In Sections 4 and 5, the microscopic fracture energy g_{f}

was calibrated imposing that at onset of cracking the macroscopic stress is the same as observed experimentally in a uniaxial tensile test (Eq. 13).

Charpin and Ehrlacher (2014) propose to consider the microscopic fracture energy as an input parameter not linked to the tensile properties of the undamaged concrete. Their scope is to model the behaviour of ASR-affected concrete in confined conditions. Their model explains the coupling between external loading and swelling of the gel in terms of concrete expansion. A high degradation of concrete stiffness for limited expansion values is reported, but a comparison with experimental findings is not made.

In this section, the proposed model is modified by adopting a similar approach. The results are obtained by calibrating only the initial aspect ratio X_{in} and considering multiples of the calibrated microscopic fracture energy g_{f}.

This approach shows an improvement in terms of expansion versus stiffness degradation, but it presents an undesired drawback in the estimation of the strengths. Figure 9a shows that the higher is the inputted microscopic fracture energy, the lower is the stiffness degradation for the same expansion level. However, a sensible difference with experimental results is still noticeable. Figure 9b reveals the major disadvantage of the method. It compares simulations of uniaxial tests performed for unaffected concrete. For high values of the inputted microscopic fracture energy, the peak stress and the ultimate strain reach unrealistic values, both in tension and compression.

In conclusion, this approach does not show any improvement and highlights once more the link between microscopic damage processes and macroscopic material deterioration.

6.2. Two-Scale Double Porosity Model

The concrete at microscopic level is known as a complex heterogeneous medium. At different observation scales, different homogeneous phases can be identified. At millimeter scale, cement paste and aggregates appear as uniform materials. On the contrary, at higher magnification, they occur as porous media. The aggregate and cement paste contains pores, which can influence the overall behaviour of the material. Their size is usually one order of magnitude smaller than the one of capillary pores, thus of microcracks (Neville et al., 1963).

The influence on the concrete behaviour of a second porosity system, at lower scale than the cracks, is investigated in this section. This approach is adopted in refined literature models, such as Ulm et al. (2014) and Pichler and Hellmich (2011), to estimate the evolution of stiffness properties during the hydration process of concrete. Here the two-scale double porosity model proposed by Dormieux et al. (2006) is adopted (Figure 10). As for the single porosity model presented in Section 2, it is assumed that the microstructure is fully saturated. As a consequence, diffusion mechanisms and gradual filling of pores are not addressed. At lower scale (level I) spherical pores are embedded in the solid matrix, which is composed by aggregates and cement paste. The resulting porous matrix is the medium in which the cracks are embedded and propagating (level II). The state equations of the system at level II read (Dormieux et al., 2006; Ulm, 2014):

$$\boldsymbol{\Sigma} = \mathbb{C} : \boldsymbol{E} - \boldsymbol{B}_{\mathrm{p}} P_{\mathrm{p}} - \boldsymbol{B}_{\mathrm{c}} P_{\mathrm{c}} \tag{16a}$$

$$\phi_{\mathrm{p}} - \phi_{\mathrm{p}}^{*} = \boldsymbol{B}_{\mathrm{p}} : \boldsymbol{E} + \frac{P_{\mathrm{p}}}{N_{\mathrm{pp}}} + \frac{P_{\mathrm{c}}}{N_{\mathrm{pc}}} \tag{16b}$$

$$\Phi - \Phi^{*} = \boldsymbol{B}_{\mathrm{c}} : \boldsymbol{E} + \frac{P_{\mathrm{p}}}{N_{\mathrm{cp}}} + \frac{P_{\mathrm{c}}}{N_{\mathrm{cc}}} \tag{16c}$$

The indexes p and c denote pores and cracks, respectively. The Biot tensors and moduli are defined as:

$$\boldsymbol{B}_{\mathrm{p}} = \boldsymbol{B}_{\mathrm{p}}^{\mathrm{pm}} : \mathbb{C}_{\mathrm{m}}^{-1} : \mathbb{C}_{\mathrm{pm}} \tag{17a}$$

$$\boldsymbol{B}_{\mathrm{c}} = \boldsymbol{I} - \mathbb{C}_{\mathrm{pm}}^{-1} : \mathbb{C} : \boldsymbol{I} \tag{17b}$$

$$\frac{1}{N_{\mathrm{pp}}} = \boldsymbol{B}_{\mathrm{p}}^{\mathrm{pm}} : \mathbb{C}_{\mathrm{pm}}^{-1} : \left[(1 - \Phi)\, \boldsymbol{B}_{\mathrm{p}}^{\mathrm{pm}} - \boldsymbol{B}_{\mathrm{p}} \right] + \frac{1 - \Phi^{*}}{N_{\mathrm{pp}}^{\mathrm{pm}}} \tag{17c}$$

$$\frac{1}{N_{\mathrm{pc}}} = -\boldsymbol{B}_{\mathrm{p}}^{\mathrm{pm}} : \mathbb{C}_{\mathrm{pm}}^{-1} : (\boldsymbol{B}_{\mathrm{c}} - \Phi^{*} \boldsymbol{I}) \tag{17d}$$

$$\frac{1}{N_{\mathrm{cp}}} = \boldsymbol{I} : \mathbb{C}_{\mathrm{pm}}^{-1} : \left[\boldsymbol{B}_{\mathrm{p}} - (1 - \Phi^{*})\, \boldsymbol{B}_{\mathrm{p}}^{\mathrm{pm}} \right] \tag{17e}$$

$$\frac{1}{N_{\mathrm{cc}}} = (\boldsymbol{B}_{\mathrm{c}} - \Phi^{*} \boldsymbol{I}) : \mathbb{C}_{\mathrm{pm}}^{-1} : \boldsymbol{I} \tag{17f}$$

with $\mathbb{C}_{\mathrm{m}}$ and $\mathbb{C}_{\mathrm{pm}}$ the stiffness tensors of the solid and porous matrix, respectively, $\boldsymbol{B}_{\mathrm{p}}^{\mathrm{pm}}$ and $N_{\mathrm{pp}}^{\mathrm{pm}}$ the Biot tensor and modulus at level I, which can be calculated with Eq. 9.

The damage criterion is evaluated at the crack scale (level II) , accounting for the interaction between the pressure in the pores P_{p} and in the cracks P_{c}. The energy release rate of the i-th crack family is evaluated as:

$$G_i = -\frac{1}{2}\langle \boldsymbol{E} \rangle : \frac{\partial \mathbb{C}}{\partial \epsilon_i} : \langle \boldsymbol{E} \rangle + \left(\boldsymbol{B}_{\mathrm{p}}^{\mathrm{pm}} : \mathbb{C}_{\mathrm{pm}}^{-1} : \frac{\partial \mathbb{C}}{\partial \epsilon_i} P_{\mathrm{p}} - \boldsymbol{I} : \mathbb{C}_{\mathrm{pm}}^{-1} : \frac{\partial \mathbb{C}}{\partial \epsilon_i} P_{\mathrm{c}} \right) : \langle \boldsymbol{E} \rangle + \\ - \boldsymbol{B}_{\mathrm{p}}^{\mathrm{pm}} : \mathbb{C}_{\mathrm{pm}}^{-1} : \frac{\partial \mathbb{C}}{\partial \epsilon_i} : \mathbb{C}_{\mathrm{pm}}^{-1} : \boldsymbol{B}_{\mathrm{p}}^{\mathrm{pm}} \frac{P_{\mathrm{p}}^2}{2} - \boldsymbol{I} : \mathbb{C}_{\mathrm{pm}}^{-1} : \frac{\partial \mathbb{C}}{\partial \epsilon_i} : \mathbb{C}_{\mathrm{pm}}^{-1} : \boldsymbol{I} \frac{P_{\mathrm{c}}^2}{2} + \\ + \left(\boldsymbol{B}_{\mathrm{p}}^{\mathrm{pm}} : \mathbb{C}_{\mathrm{pm}}^{-1} : \frac{\partial \mathbb{C}}{\partial \epsilon_i} : \mathbb{C}_{\mathrm{pm}}^{-1} : \boldsymbol{I} + \boldsymbol{I} : \mathbb{C}_{\mathrm{pm}}^{-1} : \frac{\partial \mathbb{C}}{\partial \epsilon_i} : \mathbb{C}_{\mathrm{pm}}^{-1} : \boldsymbol{B}_{\mathrm{p}}^{\mathrm{pm}} \right) P_{\mathrm{p}} P_{\mathrm{c}} \tag{18}$$

The critical energy release rate G_{ci} is determined with Eq. 12.

To compare the results obtained with the single porosity model (Sections 2 and 5) and the two-scale double porosity model, the calibration procedure has been slightly modified by imposing that the initial aspect ratio of the cracks is the same adopted in the former model ($X_{i,\mathrm{in}} = 0.057$, see Table 1). Consequently the initial volume fraction, $\phi_{\mathrm{c,in}} = \phi_{\mathrm{c1,in}} = \phi_{\mathrm{c2,in}} = \phi_{\mathrm{c3,in}}$, of the cracks has been calibrated to match the initial elastic modulus of the overall material (Table 3). The microscopic fracture energy g_{f} is determined with Eq. 13, as described in Section 4.1. The volume fraction of spherical pores ϕ_{p} is an input parameter, but its value is limited by the initial volume fraction of cracks Φ_{in} and by the overall initial stiffness Y_{in}.

Figure 11a compares the results obtained for different value of the volume fraction of spherical pores ϕ_{p}, while Figure 11b considers different ratios between the pressures $P_{\mathrm{p}}/P_{\mathrm{c}}$ in the two porosities. The two-scale double porosity model does not show appreciable difference with respect to the single porosity model. This can be explained by the evolution of Biot tensor $\boldsymbol{B}_{\mathrm{p}}$ (Figure 12), which can be directly related to the evolution of the volume fractions. In fact, the volume fraction of spherical pores f_{p} at level I is linked to the one of the cracks Φ (for more details see Chapter 5 in Dormieux et al.

(2006)):

$$f_{\mathrm{p}} = \phi_{\mathrm{p}} \left(1 - \Phi\right) \tag{19}$$

As a consequence, both the stiffness $\mathbb{C}_{\mathrm{pm}}$ and the Biot tensor $\boldsymbol{B}_{\mathrm{p}}^{\mathrm{pm}}$ of the porous matrix decrease leading to a substantial reduction of $\boldsymbol{B}_{\mathrm{p}}$.

6.3. Solidification Model

The swelling of concrete is the major effect induced by the ASR process. It is a direct consequence of the gel's expansion in a confined environment. However, the deterioration of concrete appears to be a more complex phenomenon. Previous sections showed that considering only the effect of an internal pressure P is not sufficient to correctly link the macroscopic expansion and degradation of concrete.

Experimental investigations revealed that the viscoelastic properties of the gel play an important role in the phenomena (Hagelia, 2010; Kawamura and Iwahori, 2004). It can be hypothesized that during the process the gel is changing in phase and increasing its mechanical contribution to the overall concrete material. Furthermore, in structures with major signs of deterioration, expulsion of a dense material was found on their surfaces.

Inspired by the work of Coussy (2005) for freezing materials, a model modification is presented in this section to describe the possible contribution of coexisting fluid and solid gel phases to the overall stiffness of the material. This approach should not be confused with the solidification model proposed by Bazant to describe the creep phenomenon in concrete. The ASR damage process is simulated by means of two subsequent phenomena: swelling and

solidification of the gel. The first process defines the macroscopic expansion of concrete, while the second delays the deterioration. At the beginning, the cracks are saturated by a fluid exerting an internal pressure P on the material. The concrete is modelled as a porous medium and its state equations are described by Eq. 5. Afterwards, the cracks become partially filled by a solid gel phase, characterized by an elastic modulus Y_{gel}. The i-th crack family is composed by n_{f} pressurized cracks, with volume fraction $\phi_{\mathrm{f}i}$ and n_{s} solidified cracks, with volume fraction $\phi_{\mathrm{s}i}$, where $n = n_{\mathrm{f}} + n_{\mathrm{s}}$ and $\phi_{\mathrm{c}i} = \phi_{\mathrm{f}i} + \phi_{\mathrm{s}i}$. During both processes each family has the same crack radii a, volume fraction ϕ_{c} and solidification ratio $\rho_{\mathrm{s}} = \phi_{\mathrm{s}}/\phi_{\mathrm{c}}$.

For a certain value of damage a and of solidification ρ_{s} the state equations of the system are:

$$\boldsymbol{\Sigma} = \mathbb{C} : \boldsymbol{E} - \boldsymbol{B}_{\mathrm{f}} P \tag{20a}$$

$$\Phi_{\mathrm{f}} - \Phi_{\mathrm{f}}^{*} = \boldsymbol{B}_{\mathrm{f}} : \boldsymbol{E} + \frac{P}{N_{\mathrm{f}}} \tag{20b}$$

$$\Phi_{\mathrm{s}} - \Phi_{\mathrm{s}}^{*} = \boldsymbol{B}_{\mathrm{s}} : \boldsymbol{E} \tag{20c}$$

where $\Phi_{\mathrm{f}} - \Phi_{\mathrm{f}}^{*}$ and $\Phi_{\mathrm{s}} - \Phi_{\mathrm{s}}^{*}$ are the elastic deformations of the total pressurized ($\Phi_{\mathrm{f}} = \sum_{i=1}^{m} \phi_{\mathrm{f}i}$) and solidified ($\Phi_{\mathrm{s}} = \sum_{i=1}^{m} \phi_{\mathrm{s}i}$) porosities, respectively. The overall stiffness tensor $\mathbb{C}$ is evaluated with Eq. 6 accounting for the stiffness of the solid gel phase ($\mathbb{C}_{\mathrm{f}i} = \mathbb{O}$ and $\mathbb{C}_{\mathrm{s}i} = \mathbb{C}_{\mathrm{gel}}$). The Biot tensors are evaluated as a function of the strain concentration tensor:

$$\boldsymbol{B}_{\mathrm{j}} = \sum_{i=1}^{m} \phi_{\mathrm{j}i} \mathbb{A}_{\mathrm{j}i} \;\; \text{with} \;\; \mathrm{j} = \mathrm{cp}, \mathrm{cs} \tag{21}$$

The Biot modulus of pressurized cracks N_{f} is calculated with Eqs. 21 and 9(b). The damage evolution of the i-th family is governed by the energy release rate G_i and its critical value G_{ci}, which are evaluated by Eq. 11 and 12, respectively.

Considering a porous medium, subject to an internal pressure P, in which the empty cracks are transformed in solid inclusions, an incremental formulation is needed to evaluate the state equations. The total macroscopic strain in absence of external loading $\boldsymbol{E} = \boldsymbol{E}^p$, corresponding to a crack radius $a+\delta a$ and volume fraction of solidified cracks $\Phi_{\mathrm{s}} + \delta\Phi_{\mathrm{s}}$, can be defined as:

$$\begin{aligned}
\boldsymbol{E}_{a+\delta a}^{\Phi_{\mathrm{s}}+\delta\Phi_{\mathrm{s}}} &= \left(\mathbb{D}_a^{\Phi_{\mathrm{s}}} + \delta\mathbb{D}\right) : \left(\boldsymbol{B}_a^{\Phi_{\mathrm{s}}} + \delta\boldsymbol{B}\right)(P_a + \delta P) + \\
&\quad - \underbrace{\left[\delta\mathbb{D}_a^{\delta\Phi_{\mathrm{s}}} : \boldsymbol{B}_a^{\Phi_{\mathrm{s}}} + \delta\boldsymbol{B}_a^{\delta\Phi_{\mathrm{s}}} : \left(\mathbb{D}_a^{\Phi_{\mathrm{s}}} + \delta\mathbb{D}_a^{\delta\Phi_{\mathrm{s}}}\right)\right] P_a}_{\delta\boldsymbol{E}^*} = \\
&= \mathbb{D}_a^{\Phi_{\mathrm{s}}} : \boldsymbol{B}_a^{\Phi_{\mathrm{s}}} P_a + \delta\widehat{\boldsymbol{E}} - \delta\boldsymbol{E}^* = \boldsymbol{E}_a^{\Phi_{\mathrm{s}}} + \delta\widehat{\boldsymbol{E}} - \delta\boldsymbol{E}^*
\end{aligned} \tag{22}$$

where $\mathbb{D}_a^{\Phi_{\mathrm{s}}}$ and $\boldsymbol{B}_a^{\Phi_{\mathrm{s}}}$ are the compliance and Biot tensors of the overall material in the previous stage (a and Φ_{s}), while $\delta\mathbb{D}$ and $\delta\boldsymbol{B}$ are their increments due to solidification and cracking processes, which are defined as:

$$\delta\mathbb{D} = \left(\mathbb{D}_a^{\Phi_\mathrm{s}+\delta\Phi_\mathrm{s}} - \mathbb{D}_a^{\Phi_\mathrm{s}}\right) + \left(\mathbb{D}_{a+\delta a}^{\Phi_\mathrm{s}+\delta\Phi_\mathrm{s}} - \mathbb{D}_a^{\Phi_\mathrm{s}+\delta\Phi_\mathrm{s}}\right) = \\ = \delta\mathbb{D}_a^{\delta\Phi_\mathrm{s}} + \delta\mathbb{D}_{\delta a}^{\Phi_\mathrm{s}+\delta\Phi_\mathrm{s}} \quad (23a)$$

$$\delta\boldsymbol{B} = \left(\boldsymbol{B}_a^{\Phi_\mathrm{s}+\delta\Phi_\mathrm{s}} - \boldsymbol{B}_a^{\Phi_\mathrm{s}}\right) + \left(\boldsymbol{B}_{a+\delta a}^{\Phi_\mathrm{s}+\delta\Phi_\mathrm{s}} - \boldsymbol{B}_a^{\Phi_\mathrm{s}+\delta\Phi_\mathrm{s}}\right) = \\ = \delta\boldsymbol{B}_a^{\delta\Phi_\mathrm{s}} + \delta\boldsymbol{B}_{\delta a}^{\Phi_\mathrm{s}+\delta\Phi_\mathrm{s}} \quad (23b)$$

The strain increment is denoted by $\delta\widehat{\boldsymbol{E}} - \delta\boldsymbol{E}^*$, where the strain $\delta\boldsymbol{E}^*$ refers only to the stiffening effect due to the solid inclusions. The strain $\delta\boldsymbol{E}^*$ is introduced because the solidification is assumed as a strain-free process:

$$\boldsymbol{E}_a^{\Phi_\mathrm{s}+\delta\Phi_\mathrm{s}} := \boldsymbol{E}_a^{\Phi_\mathrm{s}} := \boldsymbol{E}_a^{\Phi_\mathrm{s}=0} \quad (24)$$

Figures 13 and 14 show the comparison between the pressure-based model, presented in Sections 2 and 5, and the solidification model. For both analysis, the initial and calibrated parameters are reported in Table 1. The additional parameters needed for the solidification model, hereafter explained, are listed in Table 3. The solidification is assumed to start at crack radius $a = 2.08$ mm and evolves with a constant ratio $\rho_\mathrm{s} = \phi_\mathrm{s}/\phi_\mathrm{c} = 0.50$. The elastic modulus of the solid gel phase is assumed equal to $Y_\mathrm{gel} = 45.0$ GPa (Leemann and Lura, 2013).

Figure 13 shows the evolution of pressurized cracks space, ϕ_f, as a function of the crack radius a. If the solidification starts, this space is suddenly reduced in agreement with the ratio ρ_s.

At onset of solidification, the overall material results stiffer due to the presence of solid gel phase, as shown in Figure 14a. As a consequence, the pressure P increases due to the confinement effect exerting by the solid gel on the fluid (Figure 14b). No increment of strain ($\delta \boldsymbol{E} = 0$) occurs due to assumption in Eq. 24.

However, as the damaging proceeds, the stiffness drastically decreases because the pressurizing effect becomes more important then the solidification one. In comparison with the pressure-based approach, the solidification model provides lower strain increments for the same crack radius a (Figure 14b). In fact, if the cracks are saturated by a fluid and subjected to an increase of internal pressure P the increment in strain is $\delta \boldsymbol{E} = \delta \widehat{\boldsymbol{E}}$. At the contrary, in presence of solidification, the incremental strain is reduced by the quantity $\delta \boldsymbol{E}^*$ ($\delta \boldsymbol{E} = \delta \widehat{\boldsymbol{E}} - \delta \boldsymbol{E}^*$). Consequently, the two approaches provide similar results in terms of degradation versus expansion and no improvement is observed in comparison with experimental results.

7. CONCLUDING REMARKS

The alkali-silica reaction in concrete can be defined as a long-term multiscale damage mechanism, which induces swelling and degradation of the material. The reaction is triggered with the formation of an expansive alkali-silica gel. The gel flows into the pores and builds up an internal pressure, while confined by the concrete skeleton. When the microstructure strength is reached, the cracking process starts and affects the macroscopic level. The performances of the overall material are thus compromised, leading to a loss in capacity of the structure and promoting other deterioration mechanisms (e.g. corrosion

of reinforcements).

To understand the deteriorating impact induced by ASR in concrete, a multiscale material model has been adopted. The approach follows the microporomechanics theory developed by Dormieux et al. (2006) and has been inspired by the work of Lemarchand et al. (2005) and of Charpin and Ehrlacher (2012). The concrete is modelled as a heterogeneous material. Its microstructure is composed by cracks embedded in a solid matrix, formed by aggregates and cement paste. The macroscopic quantities of the overall material are analytically determined adopting the concept of a representative elementary volume. The approach results in a three-dimensional smeared model, which aims to characterize the macroscopic deterioration of concrete subjected to any combination of external and internal loads.

The model is based on a limited number of input and calibrated parameters, which can be determined via micro and macroscopic laboratory investigations. The input variables can be classified in three categories, which are related to: the mechanical properties of undamaged concrete (Y_{in}, $f_{\mathrm{t,in}}$), the elastic constants of the solid matrix (Y_{cem}, Y_{agg}, $\nu_{\mathrm{cem}} = \nu_{\mathrm{agg}}$, ϕ_{agg}) and the initial status of the cracks (Φ_{in}, c). A calibration procedure is adopted to determine the initial aspect ratio of the cracks X_{in} and the microscopic fracture energy g_{f}, on the basis of the macroscopic stiffness Y_{in} and tensile strength $f_{\mathrm{t,in}}$ of undamaged concrete, respectively.

The model's assumptions have been validated by simulating the behaviour of unaffected concrete under uniaxial external loading. The model results are in good agreement with empirical formulations proposed by the Model Codes (CEB-FIP, 1993; *fib*, 2011), which are based on a statistically large

number of experimental results. The well-known stress-strain relationships are approximated in terms of peak stresses, softening/hardening shape and ultimate strains for both tension and compression. Considering that the representative elementary volume is the fracture zone, which size can be estimated as three times the maximum aggregate's diameter (Bažant and Oh, 1983a), the model is able to determine the macroscopic fracture energy in tension G_{f}. Furthermore, in the case of compressive loading, the peak stress Σ^{peak} and relation between cracking and peak stress $\Sigma^{\mathrm{prop}}/\Sigma^{\mathrm{peak}} \cong 1/3$ are estimated well.

The ASR process is modelled assuming that the porosity is saturated by an expansive alkali-silica gel, which exerts an internal pressure. The evolution of mechanical properties of ASR-affected concrete is evaluated by simulating first a free-expansion test and subsequently uniaxial loading tests. A comparison with experimental findings shows that the model overestimates the degradation of mechanical properties as a function of the expansion. On the contrary, the relationship between stiffness and strength deterioration is correctly approximated.

Eventually, to improve the model performances regarding the relation between swelling and stiffness reduction of affected concrete, three model modifications have been explored. None of them lead to promising improvements. This suggests that the assumption of elastic behaviour of each phase, thus excluding permanent deformation upon removal of internal and external loads, should be reconsidered.

In conclusion, the paper shows that the proposed model is a potentially valid tool to describe the deteriorating impact of ASR on concrete. Exten-

sions of the present model to both the reaction product and the structural level are foreseen. However, first further refinements of the present model at aggregate-to-concrete level should be considered. In particular, the coupling between the ASR and long term processes, such as creep, which can induce permanent deformation in the microstructure, should be addressed. The damage evolution in presence of permanent deformation will result in a less severe mechanical degradation, thus improving the model performances. Once this point is addressed, the micromechanical model can be refined by considering the interaction between the cracks and the aggregates, thus describing the aggregate size effect on the concrete expansion. In order to describe a more realistic phenomenon at reaction product level, the model can be improved within the framework of partially saturated medium theory. Eventually, with respect to the analytical approach, the influence of different homogenization schemes should be studied.

Acknowledgements

This work is part of the project Performance Assessment Tool for Alkali-Silica Reaction (PAT-ASR, http://pat-asr.blogspot.nl/), which is developed in the context of the IS2C program (http://is2c.nl/). The authors wish to express their thanks to the Technology Foundation (STW), the Dutch Ministry of Infrastructures and the Environment (Rijkswaterstraat), SGS and TNO DIANA BV for their financial support. The authors are grateful to the Norwegian Public Roads Administration (Statens Vegvesen) and SINTEF for their collaboration. Interesting discussions with Prof. F-J. Ulm are grateful acknowledged.

References

Alnaggar, M., Cusatis, G., Di Luzio, G., 2013. Lattice Discrete Particle Modeling (LDPM) of Alkali Silica Reaction (ASR) deterioration of concrete

structures. Cement and Concrete Composites 41, 45–59.

Anaç, C., Schlangen, E., Çopuroğlu, O., 2012. Lattice model implementation on alkali silica reaction gel expansion in a reacted concrete medium. In: The 3rd international conference on concrete repair, rehabilitation and retrofitting (ICCRRR-3). Cape Town, South Africa.

Bangert, F., Kuhl, D., Meschke, G., 2004. Chemo-hygro-mechanical modelling and numerical simulation of concrete deterioration caused by alkali-silica reaction. International Journal for Numerical and Analytical Methods in Geomechanics 28 (7-8), 689–714.

Bažant, Z., Oh, B., 1983a. Crack band theory for fracture of concrete. Matériaux et Construction 16 (3), 155–177.

Bažant, Z., Oh, B., 1983b. Microplane model for fracture analysis of concrete structures. In: Symposium on Interaction of NonNuclear Munitions with Structures. U.S. Air Force Academy, Colorado, Springs, pp. 49–53.

Bažant, Z., Steffens, A., 2000. Mathematical model for kinetics of alkali-silica reaction in concrete. Cement and Concrete Research 30 (3), 419–428.

Bažant, Z., Zi, G., Meyer, C., 2000. Fracture mechanics of asr in concretes with waste glass particles of different sizes. ASCE Journal of Engineering Mechanics 126 (3), 226–232.

Benveniste, Y., 1987. A new approach to the application of mori-tanaka theory in composite-materials. Mechanics of Materials 6 (2), 147–157.

Budiansky, B., O'Connell, R., 1976. Elastic moduli of a cracked solid. International Journal of Solids and Structures 12 (2), 81 – 97.

Capra, B., Sellier, A., 2003. Orthotropic modelling of alkali-aggregate reaction in concrete structures: numerical simulations. Mechanics of materials 35 (8), 817–830.

CEB-FIP, 1993. Model Code 1990 (MC90). Thomas Telford, London.

Charlwood, R., 1994. A review of alkali aggregate in hydro-electric plants and dams. Hydropower Dams 5, 31–62.

Charpin, L., Ehrlacher, A., 2012. A computational linear elastic fracture mechanics-based model for alkali-silica reaction. Cement and Concrete Research 42 (4), 613–625.

Charpin, L., Ehrlacher, A., 2014. Microporomechanics study of anisotropy of ASR under loading. Cement and Concrete Research 63, 143–157.

Comby-Peyrot, I., Bernard, F., Bouchard, P.-O., Bay, F., Garcia-Diaz, E., 2009. Development and validation of a 3D computational tool to describe concrete behaviour at mesoscale. application to the alkali-silica reaction. Computational Materials Science 46 (4), 1163–1177.

Coussy, O., 2005. Poromechanics of freezing materials. Journal of the Mechanics and Physics of Solids 53 (8), 1689–1718.

Deude, V., Dormieux, L., Lemarchand, E., Maghous, S., Kondo, D., 2001. A micromechanical approach to the nonlinear elastic behaviour of rocks. In: DC Rocks 2001 The 38th US Symposium on Rock Mechanics (USRMS). American Rock Mechanics Association.

Dormieux, L., Kondo, D., Ulm, F.-J., 2006. Microporomechanics. John Wiley & Sons.

Dormieux, L., Lemarchand, E., Kondo, D., Fairbairn, E., 2004. Elements of poro-micromechanics applied to concrete. Materials and Structures 37 (265), 31–42.

Dunant, C. F., Scrivener, K. L., 2010. Micro-mechanical modelling of alkalisilica-reaction-induced degradation using the {AMIE} framework. Cement and Concrete Research 40 (4), 517 – 525, special Issue: ICAAR 13, Trondheim, Norway, June 16-20, 2008.

Esposito, R., 2015. The deteriorating impact of alkali-silica reaction on concrete. expansion and mechanical properties. Ph.D. thesis, Delft University of Technology, Delft, The Netherlands.

Esposito, R., Anaç, C., Hendriks, M., Çopuroğlu, O., 2015. The influence of alkali-silica reaction on the mechanical degradation of concrete, submitted for publication in ASCE Journal of Materials in Civil Engineering.

Eurocode 2 (Ed.), 2005. EN 1992-1-1: Eurocode 2 - Design of concrete structures-Part 1-1: General rules and rules for buildings.

fib, 2011. Model Code for Concrete Structures (MC2010). International Federation for Structural Concrete (*fib*), Lausanne, Switzerland.

Giorla, A., Scrivener, K., Dunant, C., 2015. Influence of visco-elasticity on the stress development induced by alkali-silica reaction. Cement and Concrete Research 70 (0), 1–8.

Glasser, F. P., 1992. The Alkali Silica Reaction in Concrete. Blackie and Son Ltd., Ch. Chemistry of the alkali aggregate reaction, pp. 30–53.

Grimal, E., Sellier, A., Le Pape, Y., Bourdarot, E., May-June 2008. Creep, shrinkage, and anisotropic damage in alkali-aggregate reaction swelling mechanism-Part I: A constitutive model. ACI Materials Journal 105 (3), 227–235.

Hagelia, P., 2010. Chemistry of ASR-gels and pore fluids in ultra-accellerated mortar bars: evidence for si-control on gel expansion properties. In: Broekmans, M., Wigum, B. (Eds.), 13th International Conference on Alkali-Aggregate Reactions in Concrete. Trondheim, Norway, pp. 697–707.

ISO, 2010. ISO 1920-10:2010(E) Testing of concrete - Part 10: Determination of static modulus of elasticity in compression. Geneva, Switzerland.

Kawamura, M., Iwahori, K., 2004. ASR gel composition and expansive pressure in mortars under restraint. Cement and concrete composites 26 (1), 47–56.

Leemann, A., Lura, P., 2013. E-modulus of the alkali-silica-reaction product determined by micro-indentation. Construction and Building Materials 44, 221–227.

Léger, P., Côté, P., Tinawi, R., 1996. Finite element analysis of concrete swelling due to alkali-aggregate reactions in dams. Computers & structures 60 (4), 601–611.

Lemarchand, E., Dormieux, L., Ulm, F.-J., 2005. Micromechanics investigation of expansive reactions in chemoelastic concrete. Philosophical Transactions of the Royal Society A-Mathematical Physical and Engineering Sciences 363 (1836), 2581–2602.

Liuaudat, J., López, C., Carol, I., March 2014. Diffusion-reaction model for ASR: Formulation and 1D numerical implementation. In: Bićanić, N., Mang, H., Meschke, G., de Borst, R. (Eds.), Computational Modelling of Concrete Structures (EURO-C). CRC Press, Taylor & Francis Group, St Anton am Alberg.

Mazars, J., 1986. A description of micro- and macroscale damage of concrete structures. Engineering Fracture Mechanics 25 (5), 729–737.

Multon, S., Sellier, A., Cyr, M., 2009. Chemo-mechanical modeling for prediction of alkali silica reaction (ASR) expansion. Cement and Concrete Research 39 (6), 490–500.

Multon, S., Toutlemonde, F., 2006. Effect of applied stresses on alkali-silica reaction-induced expansions. Cement and Concrete Research 36 (5), 912–920.

Mura, T., 1987. Micromechanics of defects in solids. Martinus Nijhoff Publishers.

NEN, 2002. NEN-EN 12390-3 Testing hardened concrete - Part 3: Compressive strength of test specimens. Delft, The Netherlands.

NEN, 2009. NEN-EN 12390-6 Testing hardened concrete - Part 6: Tensile splitting strength of test specimens. Delft, The Netherlands.

Neville, A. M., Neville, A. M., Neville, A. M., 1963. Properties of concrete. Pitman London.

Pichler, B., Hellmich, C., 2011. Upscaling quasi-brittle strength of cement paste and mortar: A multi-scale engineering mechanics model. Cement and Concrete Research 41 (5), 467–476.

Pignatelli, R., Comi, C., Monteiro, P., 2013. A coupled mechanical and chemical damage model for concrete affected by alkali–silica reaction. Cement and Concrete Research 53, 196–210.

Poyet, S., Sellier, A., Capra, B., Foray, G., Torrenti, J.-M., Cognon, H., Bourdarot, E., 2007. Chemical modelling of alkali silica reaction: Influence of the reactive aggregate size distribution. Materials and Structures 40 (2), 229–239.

Reinhardt, H., Mielich, O., 2011. A fracture mechanics approach to the crack formation in alkali-sensitive grains. Cement and Concrete Research 41 (3), 255–262.

RILEM TC 219-ACS, September 2011. RILEM Recommended Test Method: AAR-3 - Detection of potential alkali-reactivity - 38°C test method for aggregate combinations using concrete prisms (Final draft).

Sanchez, L., Fournier, B., Jolin, M., Bastien, J., 2014. Evaluation of the stiffness damage test (SDT) as a tool for assessing damage in concrete due to ASR: Test loading and output responses for concretes incorporating fine or coarse reactive aggregates. Cement and Concrete Research 56, 213–229.

Saouma, V., Perotti, L., 2006. Constitutive model for alkali-aggregate reactions. ACI Materials Journal 103 (3), 194–202.

Schlangen, E., Copuroğlu, O., 2010. Modeling of expansion and cracking due to ASR with a 3D lattice model. In: Fracture Mechanics of Concrete and Concrete Structures (FramCos7). Korea Concrete Institute, Seoul, Korea.

Suwito, A., Jin, W., Xi, Y., Meyer, C., 2002. A mathematical model for the pessimum size effect of ASR in concrete. Concrete Science and Engineering 4 (13), 23–34.

Ulm, F., Abuhaikal, M., Petersen, T., Pellenq, R., 2014. Poro-chemo-fracture-mechanics bottom-up: Application to risk of fracture design of oil and gas cement sheath at early ages. Computational Modelling of Concrete Structures, 61.

Ulm, F.-J., March 2014. Micro-poro-fracture-mechanics, personal comunication MIT/CEE/1-263.

Ulm, F.-J., Coussy, O., Li, K., Larive, C., 2000. Thermo-chemo-mechanics of asr expansion in concrete structures. ASCE Journal of Engineering Mechanics 126 (3), 233–242.

Ulm, F.-J., Petrson, M., Lemarchand, E., 2002. Is ASR-expansion caused by chemoporoplastic dilatation? Computer Science and Engineering 4 (13), 47–55.

Wu, T., Temizer, I., Wriggers, P., 2014. Multiscale hydro-thermo-chemo-mechanical coupling: Application to alkali-silica reaction. Computational Materials Science 84, 381–395.

Figures and Tables

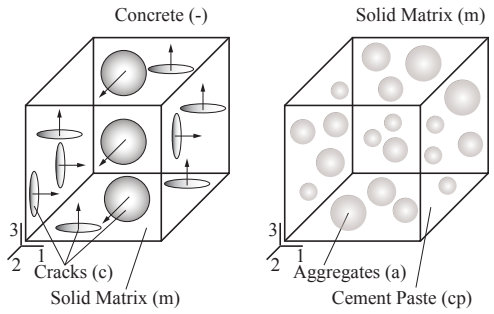

(a) (b)

Figure 1: Micromechanical model: (a) Concrete; (b) Solid matrix.

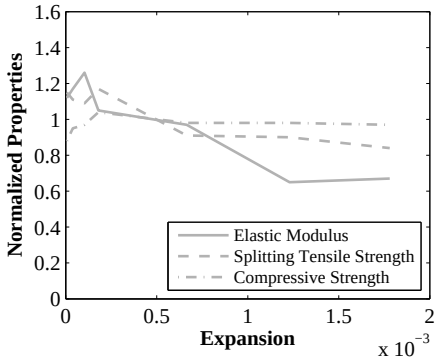

Figure 2: Case study: Degradation of elastic modulus Y, compressive strength f_{c} and splitting tensile strength $f_{\mathrm{t,sp}}$ for ASR-affected concrete in free-expansion conditions.

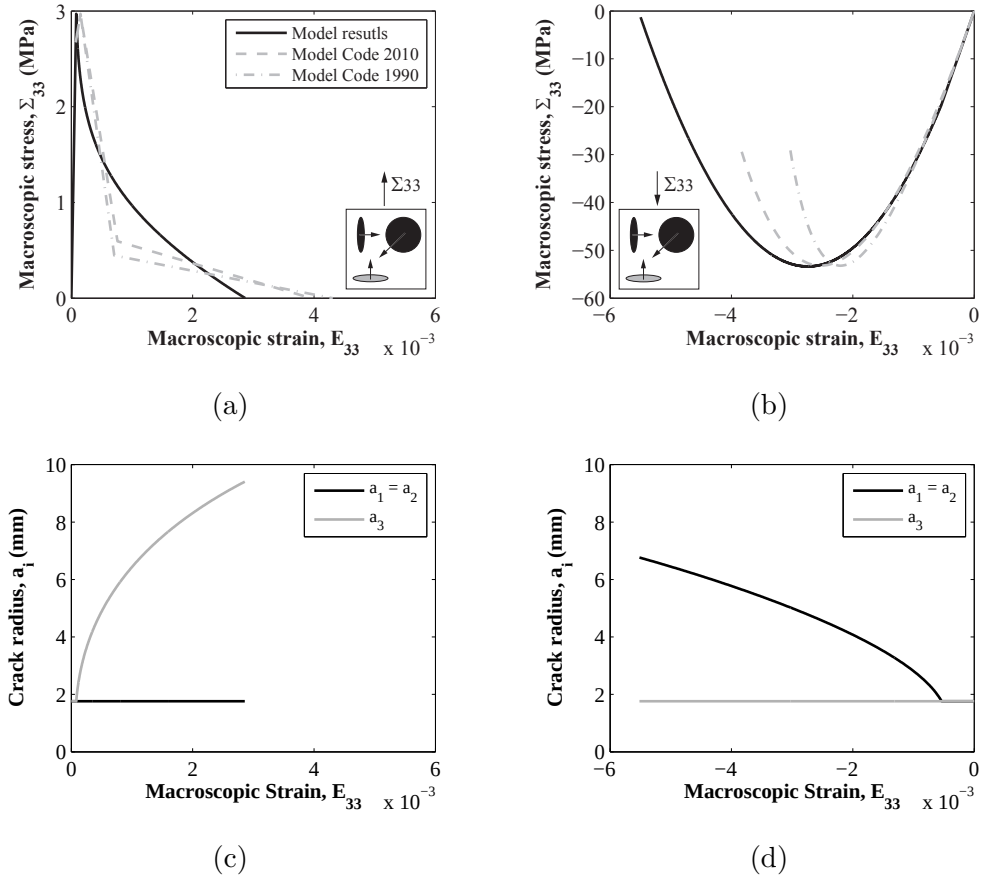

Figure 3: Degradation of concrete subjected to external mechanical loading: (a) and (c) Uniaxial tensile test; (b) and (d) Uniaxial compressive test.

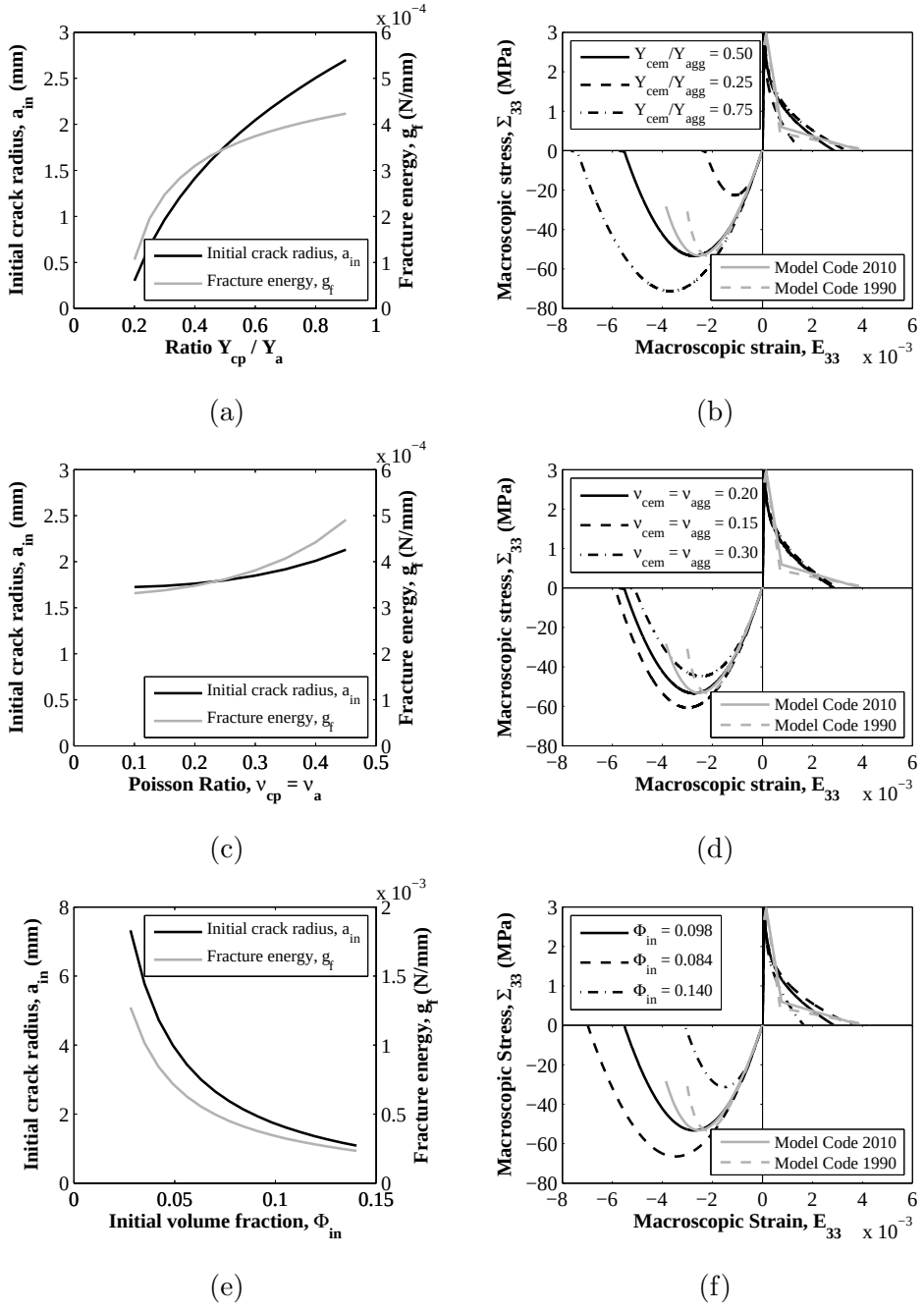

Figure 4: Parametric study: (a)-(b) Ratio between the elastic moduli of aggregates and cement paste $Y_{\mathrm{cem}}/Y_{\mathrm{agg}}$; (c)-(d) Poisson ratio $\nu_{\mathrm{cem}} = \nu_{\mathrm{agg}}$; (e)-(f) Initial volume fraction of the cracks Φ_{in}. Not scaled Y-axis in Figures (b), (d) and (f).

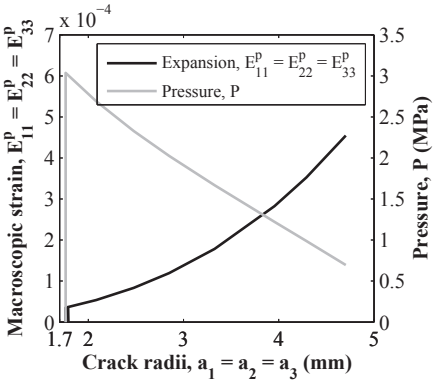

Figure 5: Concrete subjected to internal pressure: Relation between crack propagation a, pressure P and macroscopic strain $\boldsymbol{E} = \boldsymbol{E}^{\mathrm{p}}$.

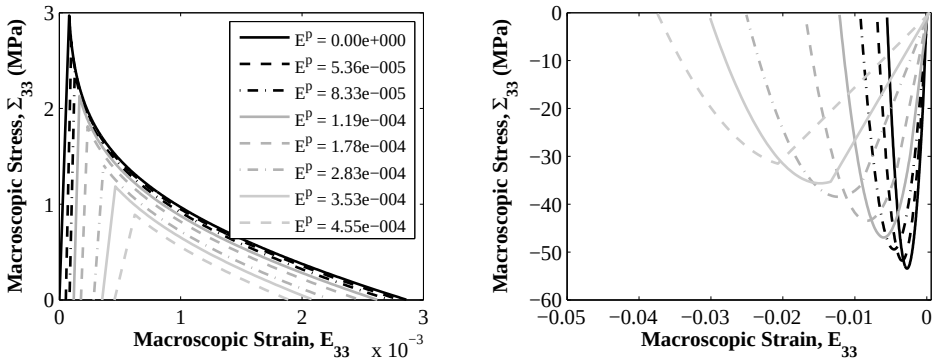

(a) (b)

Figure 6: Degradation of concrete subjected to internal pressure and subsequent mechanical loading: (a) Uniaxial tensile test; (b) Uniaxial compressive test.

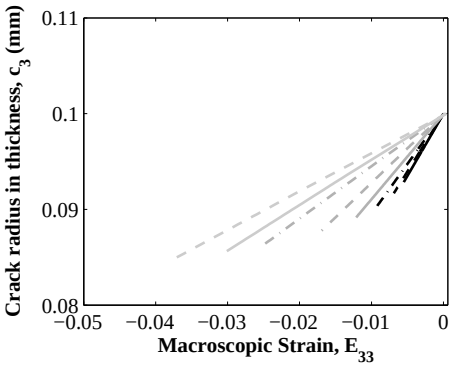

Figure 7: Degradation of concrete subjected to internal pressure and subsequent mechanical loading: Post-processing of crack closure (legend in Figure 6).

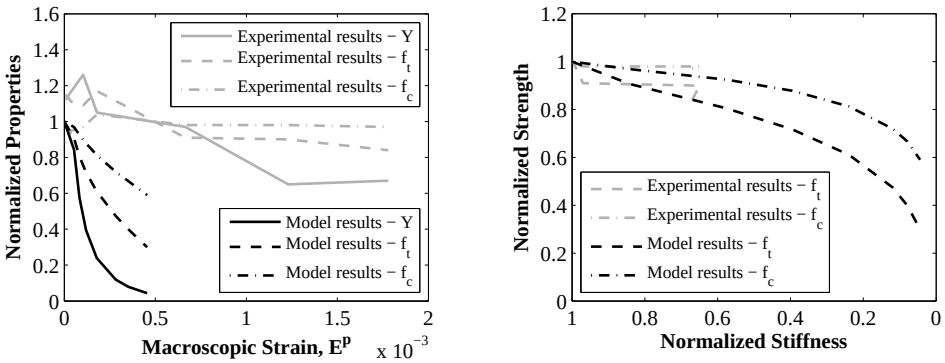

(a) (b)

Figure 8: Degradation of concrete subjected to internal pressure: (a) Degradation of Young's modulus, tensile strength and compressive strength as a function of expansion; (b) Ratio between stiffness and strengths degradation.

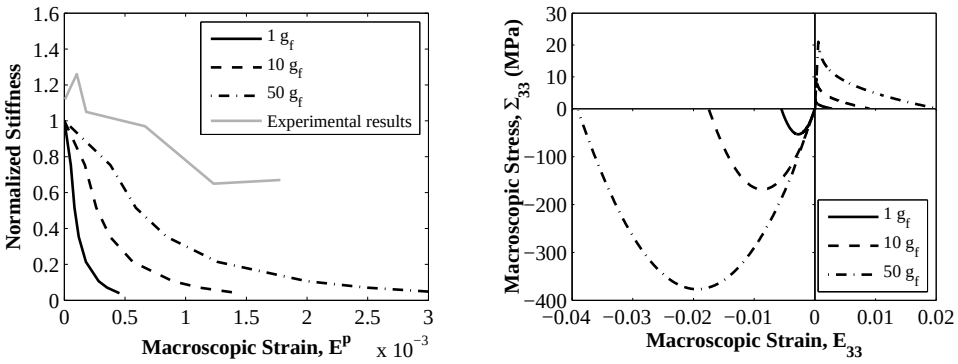

(a) (b)

Figure 9: Microscopic fracture energy: (a) Stiffness degradation due to pressure P; (b) Uniaxial test of unaffected concrete. Not scaled Y-axis in Figures (b).

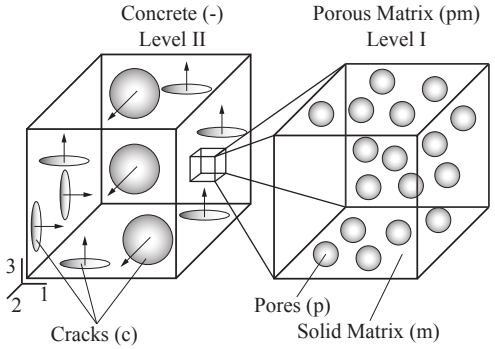

Figure 10: Two-scale double porosity model.

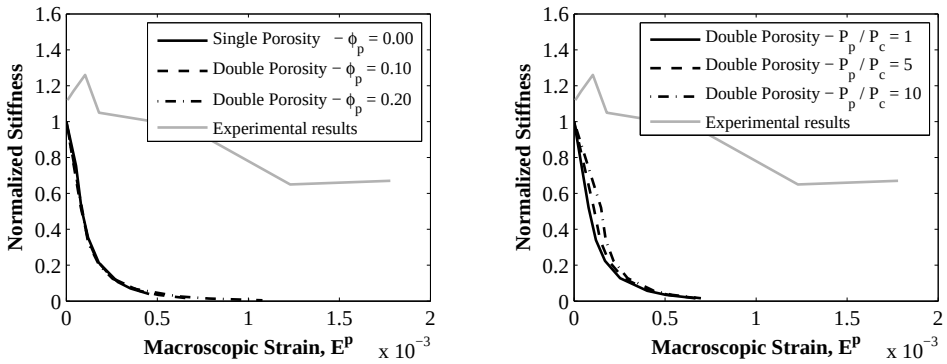

(a) (b)

Figure 11: Two-scale double porosity model: (a) Influence of the volume fraction of pores ϕ_{p} ($P_{\mathrm{p}} = P_{\mathrm{c}}$); (b) Influence of the ratio between the pressure in the pores, P_{p}, and in the cracks, P_{c} ($\phi_{\mathrm{p}} = 0.10$).

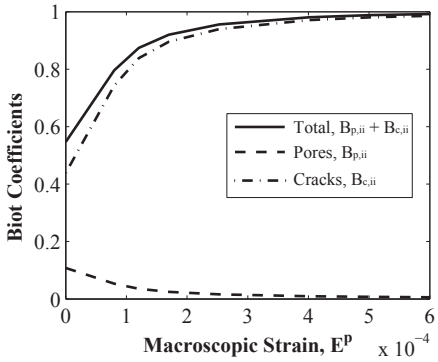

Figure 12: Two-scale double porosity model: Evolution of Biot moduli for the case $P_{\mathrm{p}} = P_{\mathrm{c}}$.

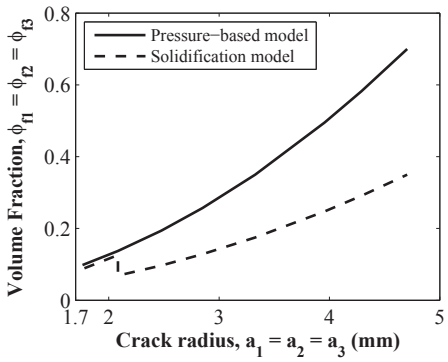

Figure 13: Comparison between pressure-based and solidification model: Evolution of pressurized cracks' space ϕ_{f}.

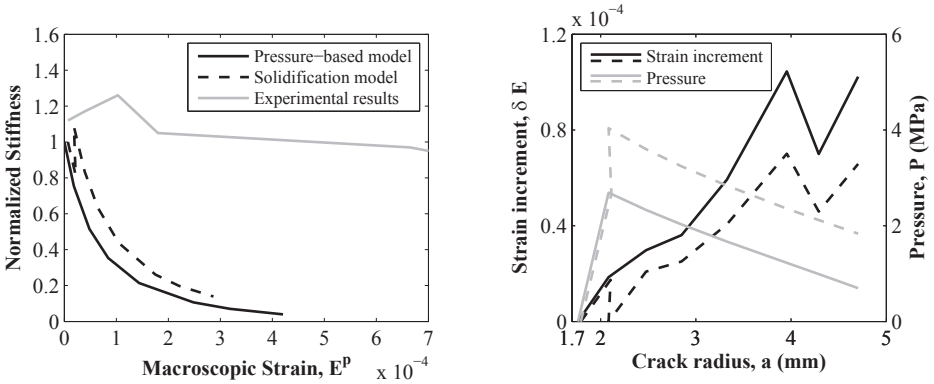

(a) (b)

Figure 14: Comparison between pressure-based and solidification model: (a) Relation between expansion and stiffness degradation; (b) Evolution of strain increment $\delta \boldsymbol{E} = \delta \widehat{\boldsymbol{E}} - \delta \boldsymbol{E}^*$ and pressure P (The legend is complementary to figure (a)).

Table 1: Input and initial parameters of the model.

Property	Unit	Value
Input parameters		
Concrete Young's modulus Y_{in}	MPa	36326*
Concrete tensile strength $f_{\mathrm{t,in}}$	MPa	2.970*
Young's modulus of cement paste Y_{cem}	MPa	43250
Young's modulus of aggregates Y_{agg}	MPa	86500
Poisson ratio $\nu_{\mathrm{cem}} = \nu_{\mathrm{agg}}$		0.200
Volume fraction of aggregate ϕ_{agg}		0.680
Initial volume fraction of cracks $\Phi_{\mathrm{in}} = 3\phi_{ci,\mathrm{in}}$		0.098
Crack thickness c_i $(i = 1, 2, 3)$	mm	0.100
Calibrated parameters		
Initial aspect ratio $X_{i,\mathrm{in}}$ $(i = 1, 2, 3)$		0.057
Microscopic fracture energy g_{f}	N/mm	$3.48\ 10^{-4}$
Dependent parameters		
Young's modulus of solid matrix Y_{m}	MPa	68603
Poisson ratio of solid matrix ν_{m}		0.200
No. of cracks n_i $(i = 1, 2, 3)$	mm^{-3}	0.025
Initial crack radius $a_{i,\mathrm{in}}$ $(i = 1, 2, 3)$	mm	1.762
Initial crack density $\epsilon_{i,\mathrm{in}}$ $(i = 1, 2, 3)$		0.138

* calculated from 28-day cubic compressive strength (Eurocode 2, 2005).

Table 2: Non-linear behaviour of concrete under mechanical loading.

Property	Unit	Value
Concrete properties		
Concrete compressive strength $f_{c,in}$	MPa	53.21*
Concrete Young's modulus Y_{in}	MPa	36326*
Concrete tensile strength $f_{t,in}$	MPa	2.97*
Maximum aggregate diameter d_{max}	mm	22.00
Calculated values using code standards		
Macroscopic fracture energy		
$G_f = 0.041(f_{c,in}/10)^{0.7}$	N/mm	0.131
$G_f = 0.073 f_{c,in}^{0.18}$	N/mm	0.149
Obtained values from the simulation		
Tensile behaviour		
$A_t = \int_0^\infty \Sigma_{33} dE_{33}$	MPa	$2.33 \ \ 10^{-3}$
$G_f = 3 d_{max} A_t$	N/mm	0.154
Compressive behaviour		
Σ_{33}^{peak}	MPa	53.29
Σ_{33}^{prop}	MPa	19.66
$\Sigma_{33}^{prop}/\Sigma_{33}^{peak}$		0.36
$A_c = \int_0^\infty \Sigma_{33} dE_{33}$	MPa	$1.96 \ \ 10^{-1}$
A_c/A_t		84.36

* calculated from 28-day cubic compressive strength (Eurocode 2, 2005).

Table 3: Complementary initial parameters for the two-scale double porosity model and the solidification model (see also Table 1).

Property	Unit	Value		
Two-scale double porosity model				
Volume fraction of pores ϕ_{p}		0	0.10	0.20
Initial aspect ratio $X_{i,\mathrm{in}}$ $(i = 1, 2, 3)$		0.057	0.057	0.057
Microscopic fracture energy g_{f}	N/mm	$3.48\ 10^{-4}$	$4.23\ 10^{-4}$	$5.20\ 10^{-4}$
No. of cracks n_i $(i = 1, 2, 3)$	mm^{-3}	0.025	0.016	0.007
Initial crack density $\epsilon_{i,\mathrm{in}}$ $(i = 1, 2, 3)$		0.138	0.085	0.041
Solidification model				
Solidification ratio ρ_{s}		0.50		
Young's modulus solid gel Y_{gel}	MPa	45000		
Start solidification a_i $(i = 1, 2, 3)$	mm	2.08		